

Probing Two-body Bound States in the Continuum and Nonlinear Breathers Using Intensity Correlations

Trideb Shit,¹ Rishav Hui,¹ Marco Di Liberto,^{2,3} Diptiman Sen,⁴ and Seabrat Mukherjee^{1,*}

¹*Department of Physics, Indian Institute of Science, Bangalore 560012, India*

²*Dipartimento di Fisica e Astronomia “G. Galilei” & Padua Quantum Technologies Research Center, Università degli Studi di Padova, I-35131 Padova, Italy*

³*Istituto Nazionale di Fisica Nucleare (INFN), Sezione di Padova, I-35131 Padova, Italy*

⁴*Centre for High Energy Physics, Indian Institute of Science, Bangalore 560012, India*

(Dated: February 29, 2024)

We study Hanbury Brown-Twiss spatial intensity correlations in femtosecond laser-fabricated photonic Su-Schrieffer-Heeger lattices. We first probe edge bound states in the continuum (BICs) of two indistinguishable bosons by mapping the intensity correlations to the two-body bosonic quantum walk. These two-body edge BICs show remarkable robustness in the presence of disorder. The localization of intensity correlation, observed in the linear regime, persists at weak nonlinearity due to the formation of *long-lived breathers* and solitons on the edge of the lattice. For stronger nonlinearities, the light tends to be delocalized from the edge site into the bulk, destroying the localization of the intensity correlation. Our results show the interplay of band structure, initial state, and nonlinearity influencing transport and intensity correlations.

Introduction.— Transport and localization in discrete lattices reveal various intriguing phenomena influenced by system parameters, gauge fields, interactions, and nonlinearity. In recent years, engineered photonic and ultra-cold atomic systems [1, 2] have found widespread applications in predicting and observing such effects, including quantum walk [3, 4], Anderson localization [5, 6], two-body physics [7–9], and topologically protected transport [10–12]. Specifically, photonic lattices consisting of evanescently coupled waveguides have become a natural platform for quantum simulation [13] due to the recent advancements in fabrication and probing methods.

A rich variety of physical phenomena can be accessed by measuring intensity correlations, as demonstrated by the seminal results of Hanbury Brown and Twiss stellar interferometry [14, 15]. Such kind of measurements have inspired novel detection techniques in various fields, including quantum optics [16–18], quantum statistics of many-body systems [19, 20], and high-energy particle physics [21, 22]. In optics, it is of great interest to understand how two-point correlations manifests when the optical fields propagate through an engineered medium rather than free space. In periodic photonic structures, light transport and intensity correlations can be strongly influenced by the photonic bands and the input state. Additionally, the quantum nature of light [23, 24] and nonlinear light-matter interactions [25] can give rise to highly non-intuitive effects.

In this work, we measure spatial intensity correlations to probe two-particle bound states in the continuum (BICs) [26–31] and long-lived discrete breathers [32–36] in a photonic SSH lattice [37–41] – i.e., a one-dimensional waveguide array with bipartite weak and strong couplings. We note that BICs are localized states embedded in a band of delocalized states that have been mostly explored in the single-particle regime;

see also Ref. [42–46]. On the other hand, discrete breathers are spatially localized nonlinear states that are periodic along the propagation distance (i.e., the analogous ‘time,’ in our case). The periodic oscillations of intensity make breathers distinct from solitons, which are shape-preserving nonlinear states [47–50]. By launching coherent optical states at two desired sites near the edge of the lattice and performing phase-averaged measurements, we obtain the intensity correlations as a function of optical power. In the linear regime, the presence of topological edge modes results in a strong localization at the corner of the correlation matrix. By mapping such measurements with the quantum walk of two indistinguishable bosons, we show that the strong localization in intensity correlation occurs due to the presence of edge BICs (here, the continuum is formed by a two-body bulk band), which are robust against small disorder. At weak optical nonlinearities, the localization of intensity correlation persists due to the formation of discrete breather-like nonlinear solutions and solitons on the edge of the lattice. When the nonlinear strength is further increased, the peak at the corner of the correlation matrix is destroyed. Such a localization-to-delocalization feature does not occur in a lattice with homogeneous couplings because no edge modes exist in the linear band structure in this case.

Model.— In the scalar-paraxial approximation, the transport of optical fields in a photonic lattice can be described by the following discrete nonlinear Schrödinger equation

$$i \frac{\partial}{\partial z} \psi_j(z) = \sum H_{jj'}^{\text{lin}} \psi_{j'} - |\psi_j|^2 \psi_j, \quad (1)$$

where the propagation distance plays the role of time ($z \leftrightarrow t$), ψ_j is proportional to the slowly-varying complex amplitude of the optical field at the j th waveguide, and

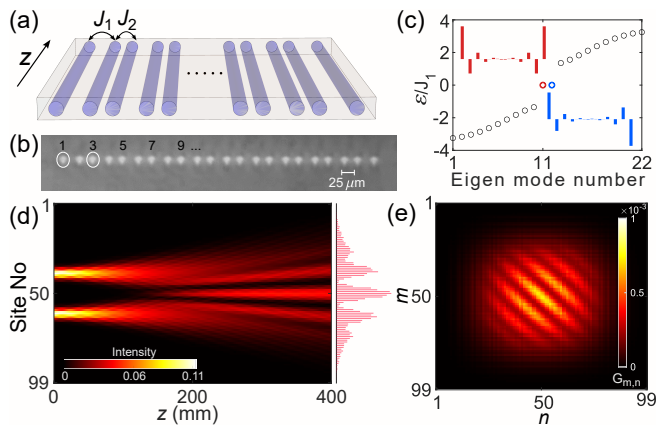


Figure 1. (a) Sketch of a photonic SSH lattice terminated with weak couplings $J_1 < J_2$. The couplings are experimentally controlled by varying the inter-site spacing. (b) Micrograph of the cross-section of a fs laser-written SSH lattice. (c) Spectrum of the SSH lattice (open circles). Notice the appearance of the edge modes in the band gap. The inset shows the real-space amplitude profiles of the edge modes. (d) Young's double slit-type interference fringes are created during light propagation through a photonic SSH lattice. These fringes disappear if the relative phase of the initial states fluctuates rapidly. (e) In a phase-averaged detection, the intensity correlation $G_{m,n}(z=400 \text{ mm})$ exhibits fringes.

H^{lin} is the linear tight-binding Hamiltonian containing the evanescent couplings and onsite energies (i.e., propagation constants). In the absence of optical loss, the total energy and the renormalized power ($g \equiv \sum_j |\psi_j|^2$) are conserved. Here, g quantifies the strength of nonlinearity, which is negligible at low optical powers.

Fig. 1(a) shows a schematic of a photonic SSH lattice with dimerized nearest-neighbor couplings $J_{1,2}$ and equal onsite energies. With periodic boundary conditions, the SSH lattice supports two linear energy bands $\varepsilon_{\pm}(k) = \pm\sqrt{J_1^2 + J_2^2 + 2J_1J_2\cos(ka)}$, where k is the quasi-momentum, and a is the lattice constant. The two dimerizations of the SSH lattice (i.e., $J_1 > J_2$ and $J_1 < J_2$) have the same spectrum; however, the nontrivial topology of the Bloch bands is reflected by the Zak phase [51] difference that can be shown to be π . For a finite lattice, topological modes appear on the boundaries when the lattice is terminated with weak couplings. In experiments, an SSH waveguide array consisting of $N = 22$ sites is created using fs laser-writing [52, 53] in an 80-mm-long borosilicate (BK7) glass substrate; see Fig. 1(b). At 1030 nm wavelength of light, the couplings were measured to be $J_1 = 0.042 \text{ mm}^{-1}$ and $J_2 = 0.096 \text{ mm}^{-1}$ – these couplings have been used in all calculations unless otherwise mentioned. The band structure of the finite lattice is presented in Fig. 1(c), where the insets show the distribution of the edge modes along the lattice.

Intensity correlation.– The spatial intensity correlation at a propagation distance z of a photonic lattice can

be defined as

$$G_{m,n}(z) = \langle I_m(z)I_n(z) \rangle, \quad (2)$$

where $I_m = |\psi_m(z)|^2 / \sum |\psi_m(z)|^2$ is the normalized intensity at the m th site, and $\langle \cdot \rangle$ denotes phase averaging from 0 to 2π . To gauge the physical significance of $G_{m,n}$, let us first consider an initial state of two equally intense broad Gaussian wave packets (as shown in Fig. 1(d)) with a relative phase $\phi = 0$. After some linear propagation, these two wave packets interfere and produce discrete interference fringes, as shown in Fig. 1(d). Averaging over initial relative phases completely washes out these interference fringes in the intensity distribution. However, the fact that interference has taken place can be still inferred from the intensity correlations, as shown in Fig. 1(e). Note that such broad initial states excite the low-energy eigenstates of the lattice, and hence, $G_{m,n}$ does not carry the full information of the band structure in this case. The width of the wave packets can be reduced to make the influence of the band structure apparent. In fact, from now on we will consider equally intense single-site excitation at the edge waveguides with a tunable relative phase.

In experiments, we launch temporally synchronized laser pulses at 1030 nm wavelength into two desired sites of the photonic lattice. Before coupling to the lattice, one of the pulses travels through a 1 mm thick glass plate that was rotated to vary the relative phase ϕ with a standard deviation of $\Delta\phi = \pi/30$. The pulse energy and phase of the input excitation are precisely controlled, and the output intensity distributions are measured using a CMOS camera; see more details in the Supplementary Material.

Two-body edge BICs.– The evolution of certain two-body quantum states of light through a photonic lattice can be captured by intensity correlations [18, 54]. Indeed, the quantum walk of two indistinguishable bosons (photons) can be emulated by probing the intensity correlation in Eq. 2 in the linear regime. When the two bosons are initially located at site p and q ($\neq p$), the modulus square of the two-body wave function is given by [55]

$$|\Psi_{m,n}(z)|^2 = \frac{1}{2} [4G_{m,n} - I_m^p I_n^p - I_m^q I_n^q], \quad (3)$$

where I_m^p is the intensity at the m th site for the initial excitation at the p site only. In other words, by measuring all three terms on the right-hand side of Eq. 3, we obtain $|\Psi_{m,n}|^2$, the probability of detecting one photon at site m and one photon at site n at the output of the lattice.

The two-body energy spectrum of a finite SSH chain terminated with weak couplings is shown in Fig. 2(a). Three bands of delocalized bulk states are indicated in blue, and another two bands of states associated with one particle on the edge and one in the bulk are shown by

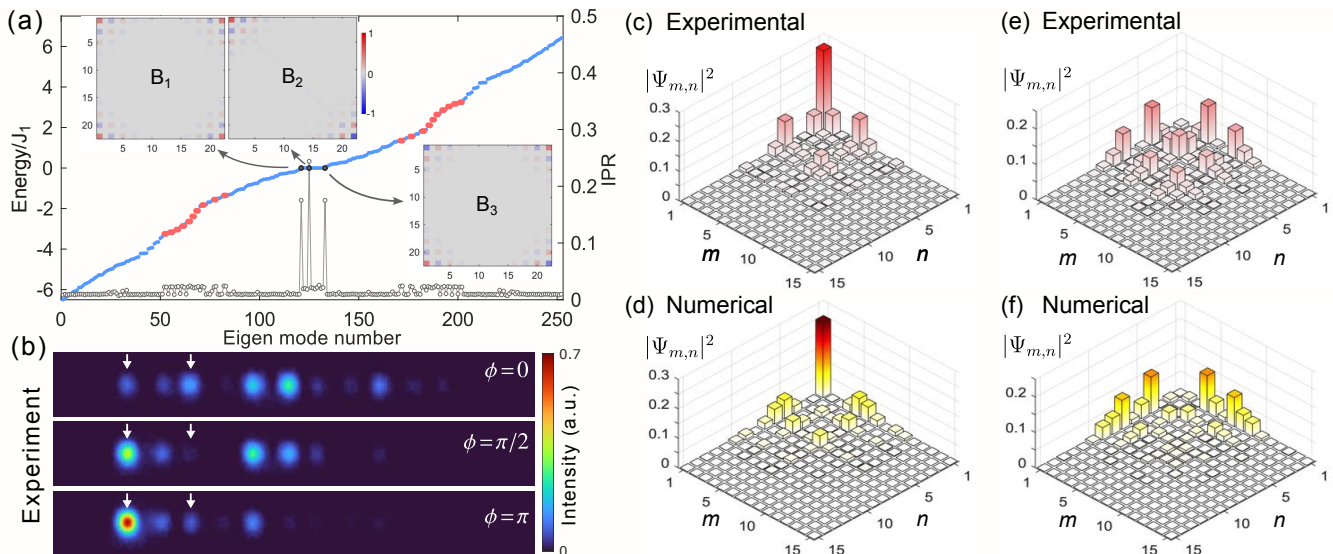


Figure 2. (a) Two-body energy spectrum (filled circles) and the IPR of the eigenstates (open circles) of the SSH lattice consisting of 22 sites and terminated with weak couplings. The two-body edge BICs are indicated by black circles and their wave functions are shown in the insets. Here $J_{1,2} = \{0.042, 0.096\} \text{ mm}^{-1}$. (b) Measured output intensity patterns at $z = 80$ mm for three different relative phases $\phi = 0, \pi/2$ and π . White arrows indicate sites 1 and 3, where the light was coupled initially. (c, d) Probing two-body edge BICs. Experimentally obtained $|\Psi_{m,n}(z = 80 \text{ mm})|^2$ agrees with numerical results. (e, f) Excitation of the semi-localized red-colored states in (a) associated with one particle on the edge and one in the bulk.

filled red circles. In the same Fig. 2(a), we quantify the localization of each eigenstate $\Phi_{m,n}$ by plotting the inverse participation ratio, $\text{IPR} \equiv \sum |\Phi_{m,n}|^4 / (\sum |\Phi_{m,n}|^2)^2$. The three most localized states (B_1, B_2 and B_3 , indicated by the black circles) are almost degenerate at zero energy, and they are located at the edge of the lattice. These states correspond to a finite-size mixing of edge modes where two particles live on the same edge or on opposite edges [56]. These localized two-body boundary modes are in resonance with the delocalized bulk modes, and hence, they act as bound states in the continuum. The BICs possess real eigenvalues even when onsite loss is introduced in the middle of the SSH array, confirming that they are exponentially localized to the edge. Additionally, in the presence of small ($\sim J_1$) disorder in couplings and onsite energies, the BICs still exist; see Supplementary Material. From the amplitude distributions in the insets of Fig. 2(a), we can infer that the edge BICs correspond to a significant probability of finding one particle at site 1 and one at site 3. In other words, the BICs can be experimentally probed by preparing the two particles initially located at site 1 and 3, i.e., $\Psi_{1,3}^{\text{in}} = |1, 3\rangle$, as described below.

We launch coherent states of light at waveguides 1 and 3 of the SSH lattice and measure the output intensities at $z = 80$ mm as a function of the relative phase ϕ . By tuning the relative phase from 0 to 2π , we can control the overlap of the initial state with the single-particle states in this case. Due to the amplitude and phase profile of the topological edge modes (see Fig. 1(c)), their overlap with the input state is maximal (minimal) for $\phi = \pi(0)$.

Experimentally measured output intensity patterns for $\phi = 0, \pi/2$, and π are shown in Fig. 2(b). Note that the optical power located at the edge is maximal (minimal) for the initial state with $\phi = \pi(0)$ relative phase, as would be expected; see also Supplementary Figs. S5(a-c).

By performing the phase-averaged measurement, we obtain $|\Psi_{m,n}|^2$, as shown in Fig. 2(c), which is in excellent agreement with our numerical prediction, Fig. 2(d). It is evident that the probability of detecting both particles at the edge site 1, i.e., $|\Psi_{1,1}|^2$, is maximal. For $J_2 > J_1$, $|\Psi_{1,1}|^2$ first oscillates as a function of z , and then slowly approaches a nonzero value that is determined by J_2/J_1 , see Supplementary Fig. S3. In addition to the BICs, the above input state overlaps with the red-colored semi-localized states shown in the spectrum, Fig. 2(a). As a result, we notice non-zero elements $|\Psi_{1,n}|^2$ and $|\Psi_{m,1}|^2$ ($m, n \neq 1$) in Figs. 2(c, d). However, the prominent peak at $\{1, 1\}$ is due to the BICs only. To gauge the significance of the initial state and to prove that the semi-localized states do not cause a prominent peak at $\{1, 1\}$, we performed another correlation measurement by coupling light to sites 1 and 2 of the SSH lattice – the analogous two-body input state is $\Psi_{1,2}^{\text{in}} = |1, 2\rangle$. In this case, the semi-localized states in the spectrum Fig. 2(a) are efficiently excited (80%); but the excitation of the BICs is insignificant, see Supplementary Fig. S3(b). Hence, one photon penetrates the bulk and the other one lives on the boundary; however, $\Psi_{1,1}$ is insignificant, as shown in Fig. 2(e, f). We note that these BICs do not exist for $J_1 \geq J_2$ (trivial case), and we have experimentally verified this using a one-dimensional

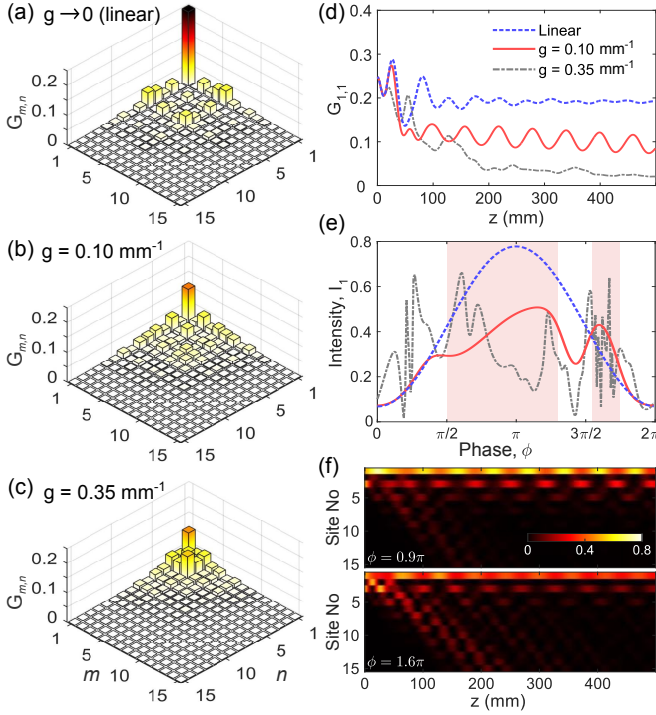


Figure 3. (a-c) Numerically obtained intensity correlations $G_{m,n}(z = 80 \text{ mm})$ in the linear, weak, and strong nonlinear regimes. (d) The variation of $G_{1,1}$ with propagation distance. (e) Intensity at waveguide 1 at $z = 80 \text{ mm}$ as a function of ϕ for three different nonlinearities. The reddish shade is a guide to the eye, indicating the phase values for which long-lived edge breathers are formed in the weak nonlinear regime, $g = 0.1 \text{ mm}^{-1}$ (red curve). (f) Dynamics of the two-site input state for $g = 0.1 \text{ mm}^{-1}$, confirming the formation of long-lived edge breathers at $\phi = 0.9\pi$ and 1.6π . Only 15 lattice sites are shown here.

waveguide array with $J_1 = J_2$.

Nonlinear effects.— Usually, when self-focusing Kerr nonlinearity is introduced in a discrete lattice, the spreading of light is reduced. Intuitively, this explains why the intensity correlations in a one-dimensional photonic lattice with homogeneous couplings exhibit a delocalization-to-localization behavior as a function of nonlinearity; see Supplementary Fig. S8. On the contrary, $G_{m,n}$ for the SSH chain shows a localization-to-delocalization feature, Fig. 3(a-c) – the peak of $G_{m,n}$ at $\{1, 1\}$ reduces as we increase the nonlinear strength. To highlight the dynamics, we plot the variation of $G_{1,1}$ with z in Fig. 3(d). In the linear case, $G_{1,1}$ reaches a fixed value after some initial transient dynamics. For $g = 0.1 \text{ mm}^{-1}$, $G_{1,1}(z)$ oscillates around a mean value that decays slowly, whereas at a larger nonlinear strength $g = 0.35 \text{ mm}^{-1}$, $G_{1,1}(z)$ decays fast along z . In other words, the peak of $G_{m,n}$ at $\{1, 1\}$ persists for weak nonlinear strengths; however, it is destroyed at a larger nonlinearity. Note that $G_{1,1}$ is the phase average of intensity square at waveguide 1, i.e., $G_{1,1} = \langle I_1^2 \rangle$. Hence, to understand the influence of nonlinearity in

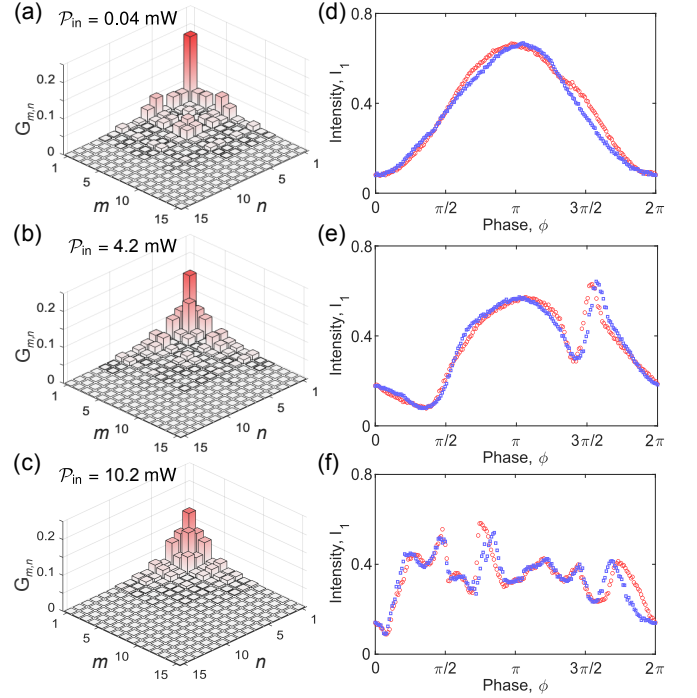


Figure 4. (a-c) Experimentally measured intensity correlation $G_{m,n}(z = 80 \text{ mm})$ at three different input powers \mathcal{P}_{in} indicated on the top of each image. Here, the field of view ($m \times n$) is smaller than the actual experiments. (d-f) Measured intensity at waveguide 1 as a function of ϕ associated with (a-c). Due to the formation of breather-like edge states, two prominent peaks are observed in (e). Data sets for two independent measurements are shown by red and blue circles.

Figs. 3(a-c), we plot I_1 as a function of ϕ for the three different nonlinear strengths, see Fig. 3(e). In the linear regime, I_1 exhibits one peak at $\phi = \pi$ because the initial state overlaps maximally with the topological edge modes in this case. As ϕ deviates from π , the bulk modes are excited more, and hence, I_1 reduces; see also Supplementary Figs. S5(a-c). It is evident that the phase average of I_1 (and hence, I_1^2) is significant in the linear case, giving rise to the prominent peak in Fig. 3(a) at the corner, $\{1, 1\}$.

The oscillatory behavior of $G_{1,1}(z)$ in the weak nonlinear regime (Fig. 3(d)) indicates the possible formation of localized nonlinear edge states *over a range of relative phases*. Indeed, the nonlinear dynamics in Supplementary Fig. S6(b-d) and Supplementary Movie 2 confirm the formation of long-lived breathers and solitons at the edge of the lattice. Additionally, $I_1(\phi)$ exhibits two peaks, see red the curve in Fig. 3(e), which are the signature of these nonlinear edge states as demonstrated experimentally (see below). In fact, the breathers form around the two peaks, i.e., near $\phi = (0.9 \pm 0.4)\pi$ and $\phi = (1.65 \pm 0.1)\pi$. The nonlinear dynamics of the two-site input state is presented in Fig. 3(f), showing the edge breathers at $\phi = 0.9\pi$ and $\phi = 1.6\pi$. As mentioned before, a discrete breather is a nonlinear state localized

along the lattice axis and periodic along z . For a true breather, one can obtain the quasienergy considering Floquet theory; see Supplementary Fig. S9. Now, for a localized nonlinear state with ≈ 58 mm period, as in the case of Fig. 3(f), the Floquet quasienergy spectrum would be gapless due to band folding [55]. In other words, these breather-like states are in resonance with the linear modes, causing their finite lifetime. We also notice the formation of edge solitons at specific phases, e.g., at $\phi = 0.3\pi$ in Supplementary Fig. S6(a). Since these edge solitons require relatively low power, most of the light was observed to penetrate in the bulk.

In the case of a larger nonlinear strength $g = 0.35$ mm $^{-1}$, the dynamics is more sensitive to relative phase ϕ , see Supplementary Fig. S6(e-h) and Supplementary Movie 3. Notice the rapid changes in $I_1(\phi)$, particularly near $\phi = \pm\pi/2$. As shown in Supplementary Movie 3, long-lived localized nonlinear edge modes are not formed for a wide range of ϕ , in this case. As a result, the peak of $G_{m,n}$ at $\{1,1\}$ is almost destroyed, Fig. 3(c). On a separate note, in the limiting case of $g \gg J_2$, the initial state will be trapped, hence, the localization of $G_{m,n}$ at $\{1,1\}$ can be restored.

To probe the above nonlinear effects, we introduce a tunable nonlinearity by using intense laser pulses with controllable pulse energy. It is worth mentioning that the unwanted effect of self-phase modulation was minimized by temporally stretching and down-chirping the laser pulses. Additionally, chromatic dispersion and multi-photon absorption were found to be negligible in our experiments. The nonlinear strength g was calibrated by characterizing two-waveguide devices and was found to be $g = 0.045 \mathcal{P}_{\text{in}}$ mm $^{-1}$ mW $^{-1}$; see Supplementary Material [55]. For the equally intense two-site excitation at waveguides 1 and 3, we measured output intensity distributions as a function of relative phase ϕ and average input power \mathcal{P}_{in} . The intensity correlations $G_{m,n}(z = 80$ mm) for three different \mathcal{P}_{in} are shown in Fig. 4(a-c), which are in good agreement with Fig. 3(a-c). The associated variations of I_1 with ϕ are shown in Fig. 4(d-f), respectively, for two independent measurements. Notice a single peak in the linear case and a double peak in the weak nonlinear regime; Fig. 4(d,e) – here data sets for two independent measurements are shown by red and blue circles. In our experiments, the second peak in $I_1(\phi)$ was observed for a range of power (2.1 mW to 4.2 mW), clearly proving the existence of the breather-like nonlinear states. When nonlinearity was further increased, more peaks started appearing – Fig. 4(f) shows the case of $\mathcal{P}_{\text{in}} = 10.2$ mW. It should be noted that the front and rare tails of the laser pulse behave linearly, giving rise to small deviations between experiments and numerics. However, by inspecting Fig. 3 and Fig. 4, we notice a good qualitative agreement.

Conclusions.— We have experimentally and numerically studied light transport and intensity correlations

in an SSH lattice. In the linear regime, the intensity correlation exhibits strong localization emulating two-body edge BICs, which are robust against small disorder. This work opens an exciting route towards the investigation of BICs in the context of few or many-body physics [42, 43]. In the nonlinear measurements, we demonstrate the formation of solitons and long-lived breathers on the edge of the topological lattice. Nonlinear interactions cause a dramatic localization and delocalization of intensity correlations that is not found in a lattice with homogeneous couplings. This work can be extended to ‘time’-modulated two-dimensional lattices for exploring intensity correlations and nonlinear dynamics in photonic topological insulators [57].

Acknowledgments.— S.M. gratefully acknowledges funding from the Indian Institute of Science (IISc) through a start-up grant. S.M. also thanks the Indian Space Research Organization (ISRO) and Science and Engineering Research Board (SERB) for funding through the ISRO-IISc Space Technology Cell (code no ISTC/PPH/SM/465) and the Start-up Research Grant (file no SRG/2022/002062), respectively. T.S. and R.H. thank IISc for scholarships through the Integrated PhD program. MDL acknowledges support by the Italian Ministry of University and Research via the Rita Levi-Montalcini program.

* mukherjee@iisc.ac.in

- [1] D. N. Christodoulides, F. Lederer, and Y. Silberberg, Discretizing light behaviour in linear and nonlinear waveguide lattices, *Nature* **424**, 817 (2003).
- [2] I. Bloch, J. Dalibard, and S. Nascimbene, Quantum simulations with ultracold quantum gases, *Nat. Phys.* **8**, 267 (2012).
- [3] H. B. Perets, Y. Lahini, F. Pozzi, M. Sorel, R. Morandotti, and Y. Silberberg, Realization of quantum walks with negligible decoherence in waveguide lattices, *Phys. Rev. Lett.* **100**, 170506 (2008).
- [4] M. Karski, L. Förster, J.-M. Choi, A. Steffen, W. Alt, D. Meschede, and A. Widera, Quantum walk in position space with single optically trapped atoms, *Science* **325**, 174 (2009).
- [5] T. Schwartz, G. Bartal, S. Fishman, and M. Segev, Transport and Anderson localization in disordered two-dimensional photonic lattices, *Nature* **446**, 52 (2007).
- [6] J. Billy, V. Josse, Z. Zuo, A. Bernard, B. Hambrecht, P. Lugan, D. Clément, L. Sanchez-Palencia, P. Bouyer, and A. Aspect, Direct observation of Anderson localization of matter waves in a controlled disorder, *Nature* **453**, 891 (2008).
- [7] G. Corrielli, A. Crespi, G. Della Valle, S. Longhi, and R. Osellame, Fractional Bloch oscillations in photonic lattices, *Nat. Commun.* **4**, 1555 (2013).
- [8] P. M. Preiss, R. Ma, M. E. Tai, A. Lukin, M. Rispoli, P. Zupancic, Y. Lahini, R. Islam, and M. Greiner, Strongly correlated quantum walks in optical lattices, *Science* **347**, 1229 (2015).

- [9] S. Mukherjee, M. Valiente, N. Goldman, A. Spracklen, E. Andersson, P. Öhberg, and R. R. Thomson, Observation of pair tunneling and coherent destruction of tunneling in arrays of optical waveguides, *Phys. Rev. A* **94**, 053853 (2016).
- [10] T. Ozawa, H. M. Price, A. Amo, N. Goldman, M. Hafezi, L. Lu, M. C. Rechtsman, D. Schuster, J. Simon, O. Zilberberg, and I. Carusotto, Topological photonics, *Rev. Mod. Phys.* **91**, 015006 (2019).
- [11] D. Smirnova, D. Leykam, Y. Chong, and Y. Kivshar, Nonlinear topological photonics, *Appl. Phys. Rev.* **7**, 021306 (2020).
- [12] M. Aidelsburger, M. Lohse, C. Schweizer, M. Atala, J. T. Barreiro, S. Nascimbène, N. Cooper, I. Bloch, and N. Goldman, Measuring the Chern number of Hofstadter bands with ultracold bosonic atoms, *Nat. Phys.* **11**, 162 (2015).
- [13] R. P. Feynman, Simulating physics with computers, *Int. J. Theor. Phys.* **21**, 10.1007/BF02650179 (1982).
- [14] R. H. Brown and R. Q. Twiss, A test of a new type of stellar interferometer on Sirius, *Nature* **178**, 1046 (1956).
- [15] R. H. Brown and R. Q. Twiss, Correlation between photons in two coherent beams of light, *Nature* **177**, 27 (1956).
- [16] H. Paul, Interference between independent photons, *Rev. Mod. Phys.* **58**, 209 (1986).
- [17] R. J. Glauber, Photon correlations, *Phys. Rev. Lett.* **10**, 84 (1963).
- [18] Y. Bromberg, Y. Lahini, R. Morandotti, and Y. Silberberg, Quantum and classical correlations in waveguide lattices, *Phys. Rev. Lett.* **102**, 253904 (2009).
- [19] M. Henny, S. Oberholzer, C. Strunk, T. Heinzel, K. Ensslin, M. Holland, and C. Schönenberger, The fermionic Hanbury Brown and Twiss experiment, *Science* **284**, 296 (1999).
- [20] T. Jelts, J. M. McNamara, W. Hogervorst, W. Vassen, V. Krachmalnicoff, M. Schellekens, A. Perrin, H. Chang, D. Boiron, A. Aspect, *et al.*, Comparison of the Hanbury Brown–Twiss effect for bosons and fermions, *Nature* **445**, 402 (2007).
- [21] H. Bøggild, J. Boissvain, M. Cherney, J. Dodd, J. Downing, S. Esumi, C. Fabjan, A. Franz, K. Hansen, T. Humanic, *et al.*, Identified pion interferometry in heavy-ion collisions at CERN, *Phys. Lett. B* **302**, 510 (1993).
- [22] G. Baym, The physics of Hanbury Brown–Twiss intensity interferometry: from stars to nuclear collisions, *Acta Phys. Pol. B* **29**, 1839 (1998).
- [23] A. Peruzzo, M. Lobino, J. C. Matthews, N. Matsuda, A. Politi, K. Poulios, X.-Q. Zhou, Y. Lahini, N. Ismail, K. Wörhoff, *et al.*, Quantum walks of correlated photons, *Science* **329**, 1500 (2010).
- [24] F. Klauck, M. Heinrich, and A. Szameit, Photonic two-particle quantum walks in Su-Schrieffer-Heeger lattices, *Photonics Res.* **9**, A1 (2021).
- [25] Y. Bromberg, Y. Lahini, E. Small, and Y. Silberberg, Hanbury Brown and Twiss interferometry with interacting photons, *Nat. Photon.* **4**, 721 (2010).
- [26] J. Von Neumann and E. Wigner, Über merkwürdige diskrete eigenwerte, *Phys. Z.* **30**, 465–467 (1929).
- [27] C. W. Hsu, B. Zhen, A. D. Stone, J. D. Joannopoulos, and M. Soljačić, Bound states in the continuum, *Nat. Rev. Mater.* **1**, 1 (2016).
- [28] Y. Plotnik, O. Peleg, F. Dreisow, M. Heinrich, S. Nolte, A. Szameit, and M. Segev, Experimental observation of optical bound states in the continuum, *Phys. Rev. Lett.* **107**, 183901 (2011).
- [29] A. Cerjan, M. Jürgensen, W. A. Benalcazar, S. Mukherjee, and M. C. Rechtsman, Observation of a higher-order topological bound state in the continuum, *Phys. Rev. Lett.* **125**, 213901 (2020).
- [30] H. Friedrich and D. Wintgen, Interfering resonances and bound states in the continuum, *Phys. Rev. A* **32**, 3231 (1985).
- [31] M. Robnik, A simple separable hamiltonian having bound states in the continuum, *J. Phys. A Math. Theor.* **19**, 3845 (1986).
- [32] S. Flach and C. R. Willis, Discrete breathers, *Phys. Rep.* **295**, 181 (1998).
- [33] G. Kopidakis and S. Aubry, Discrete breathers and delocalization in nonlinear disordered systems, *Phys. Rev. Lett.* **84**, 3236 (2000).
- [34] D. Mandelik, H. Eisenberg, Y. Silberberg, R. Morandotti, and J. Aitchison, Observation of mutually trapped multi-band optical breathers in waveguide arrays, *Phys. Rev. Lett.* **90**, 253902 (2003).
- [35] E. Trias, J. Mazo, and T. Orlando, Discrete breathers in nonlinear lattices: Experimental detection in a Josephson array, *Phys. Rev. Lett.* **84**, 741 (2000).
- [36] M. Johansson, Topological edge breathers in a nonlinear Su-Schrieffer-Heeger lattice, *Phys. Lett. A* **458**, 128593 (2023).
- [37] W. Su, J. Schrieffer, and A. J. Heeger, Solitons in polyacetylene, *Phys. Rev. Lett.* **42**, 1698 (1979).
- [38] N. Malkova, I. Hromada, X. Wang, G. Bryant, and Z. Chen, Observation of optical Shockley-like surface states in photonic superlattices, *Opt. Lett.* **34**, 1633 (2009).
- [39] S. Weimann, M. Kremer, Y. Plotnik, Y. Lumer, S. Nolte, K. G. Makris, M. Segev, M. C. Rechtsman, and A. Szameit, Topologically protected bound states in photonic parity–time-symmetric crystals, *Nat. Mater.* **16**, 433 (2017).
- [40] D. Dobrykh, A. Yulin, A. Slobozhanyuk, A. Poddubny, and Y. S. Kivshar, Nonlinear control of electromagnetic topological edge states, *Phys. Rev. Lett.* **121**, 163901 (2018).
- [41] Y. Li, Y. Wang, H. Zhao, H. Du, J. Zhang, Y. Hu, F. Mei, L. Xiao, J. Ma, and S. Jia, Interaction-induced breakdown of chiral dynamics in the Su-Schrieffer-Heeger model, *Phys. Rev. Res.* **5**, L032035 (2023).
- [42] J. Zhang, D. Braak, and M. Kollar, Bound states in the continuum realized in the one-dimensional two-particle Hubbard model with an impurity, *Phys. Rev. Lett.* **109**, 116405 (2012).
- [43] G. Della Valle and S. Longhi, Floquet-Hubbard bound states in the continuum, *Phys. Rev. B* **89**, 115118 (2014).
- [44] M. Di Liberto, A. Recati, I. Carusotto, and C. Menotti, Two-body physics in the Su-Schrieffer-Heeger model, *Phys. Rev. A* **94**, 062704 (2016).
- [45] M. A. Gorlach and A. N. Poddubny, Topological edge states of bound photon pairs, *Phys. Rev. A* **95**, 053866 (2017).
- [46] S. Sugimoto, Y. Ashida, and M. Ueda, Many-body bound states in the continuum, arXiv preprint arXiv:2307.05456 10.48550/arXiv.2307.05456 (2023).
- [47] A. Barthelemy, S. Maneuf, and C. Froehly, Propagation soliton et auto-confinement de faisceaux laser par non

- linearité optique de kerr, *Opt. Commun.* **55**, 201 (1985).
- [48] D. Christodoulides and R. Joseph, Discrete self-focusing in nonlinear arrays of coupled waveguides, *Opt. Lett.* **13**, 794 (1988).
- [49] M. Segev, B. Crosignani, A. Yariv, and B. Fischer, Spatial solitons in photorefractive media, *Phys. Rev. Lett.* **68**, 923 (1992).
- [50] H. Eisenberg, Y. Silberberg, R. Morandotti, A. Boyd, and J. Aitchison, Discrete spatial optical solitons in waveguide arrays, *Phys. Rev. Lett.* **81**, 3383 (1998).
- [51] M. Atala, M. Aidelsburger, J. T. Barreiro, D. Abanin, T. Kitagawa, E. Demler, and I. Bloch, Direct measurement of the Zak phase in topological bloch bands, *Nat. Phys.* **9**, 795 (2013).
- [52] K. M. Davis, K. Miura, N. Sugimoto, and K. Hirao, Writing waveguides in glass with a femtosecond laser, *Opt. Lett.* **21**, 1729 (1996).
- [53] A. Szameit and S. Nolte, Discrete optics in femtosecond-laser-written photonic structures, *J. Phys. B: At. Mol. Opt. Phys.* **43**, 163001 (2010).
- [54] R. Keil, A. Szameit, F. Dreisow, M. Heinrich, S. Nolte, and A. Tünnermann, Photon correlations in two-dimensional waveguide arrays and their classical estimate, *Phys. Rev. A* **81**, 023834 (2010).
- [55] See supplementary materials.
- [56] Denoting the SSH single-particle edge modes by $|L\rangle$ and $|R\rangle$, the two particle states $|L\rangle \otimes |L\rangle$, $|R\rangle \otimes |R\rangle$ and $(|L\rangle \otimes |R\rangle + |R\rangle \otimes |L\rangle)/\sqrt{2}$ are eigenstates of the two-particle noninteracting problem in the thermodynamic limit.
- [57] K. Tschernig, Á. Jimenez-Galán, D. N. Christodoulides, M. Ivanov, K. Busch, M. A. Bandres, and A. Perez-Leija, Topological protection versus degree of entanglement of two-photon light in photonic topological insulators, *Nat. Commun.* **12**, 1974 (2021).
- [58] Y. Lumer, Y. Plotnik, M. C. Rechtsman, and M. Segev, Self-localized states in photonic topological insulators, *Phys. Rev. Lett.* **111**, 243905 (2013).

Supplementary Information

Probing Two-body Bound States in the Continuum and Nonlinear Breathers Using Intensity Correlations

In the following sections of the supplementary material, we present experimental and numerical results for completeness.

Derivation of Eq. 3

In general, a tight binding Hamiltonian in the second quantization notation can be written as

$$\hat{H} = \frac{\hbar c}{n_0} \sum_{m,n=1}^N H_{nm}^{\text{lin}} \hat{a}_m^\dagger \hat{a}_n, \quad (\text{S1})$$

where \hat{a}^\dagger (\hat{a}) is the bosonic creation (annihilation) operator, \hbar is the reduced Planck constant, c is the speed of light in vacuum, n_0 is the refractive index of the medium, and H_{nm}^{lin} is the coupling strength between n -th and m -th sites. In Heisenberg picture, the evolution equation of the creation operator is given by

$$\begin{aligned} \frac{d\hat{a}_q^\dagger(t)}{dt} &= -\frac{i}{\hbar} \left[\hat{a}_q^\dagger(t), \hat{H}(t) \right], \\ \frac{d\hat{a}_q^\dagger(t)}{dt} &= -\frac{i}{\hbar} \hat{U}^\dagger(t) \left[\hat{a}_q^\dagger, \hat{H} \right] \hat{U}(t), \\ \frac{d\hat{a}_q^\dagger(z)}{dz} &= i \sum_m H_{qm}^{\text{lin}} \hat{a}_m^\dagger(z), \end{aligned} \quad (\text{S2})$$

where $\hat{H}(t) = \hat{U}^\dagger(t) \hat{H} \hat{U}(t)$ and $z = ct/n_0$. Integrating the above evolution equation, we get

$$\hat{a}_q^\dagger(z) = \sum_m U_{qm}(z) \hat{a}_m^\dagger(z=0), \quad (\text{S3})$$

where $\hat{U}(z) = e^{iz\hat{H}^{\text{lin}}}$, the explicit form of the time evolution of the creation operators. Now, the photon number correlation for a given two-photon input state initially coupled at waveguide p and $q \neq p$, i.e., $|p, q\rangle = \hat{a}_p^\dagger \hat{a}_q^\dagger |0\rangle$, at a propagation distance z is

$$\begin{aligned} \Gamma_{mn}(z) &= \langle p, q | \hat{a}_m^\dagger(z) \hat{a}_n^\dagger(z) \hat{a}_n(z) \hat{a}_m(z) | p, q \rangle \\ &= \sum_{s_1 s_2 s_3 s_4} U_{ms_1}(z) U_{ns_2}(z) U_{s_3}^*(z) U_{s_4}^*(z) \\ &\quad \times \langle p, q | \hat{a}_{s_1}^\dagger \hat{a}_{s_2}^\dagger \hat{a}_{s_3} \hat{a}_{s_4} | p, q \rangle, \\ &= |U_{mp}(z) U_{nq}(z) + U_{mq}(z) U_{np}(z)|^2. \end{aligned} \quad (\text{S4})$$

Now let us consider an initial state $\Psi_p(z=0) = 1/\sqrt{2}$ and $\Psi_q(z=0) = \exp(i\phi)/\sqrt{2}$ coupled to the lattice sites p and q , respectively, with a relative phase ϕ . In this case, the output intensity at the m th site after a propagation

of z is given by $I_m(\phi, z) = \frac{1}{2} |U_{mp}(z) + U_{mq}(z) e^{i\phi}|^2$. The intensity correlation can then be written as

$$\begin{aligned} G_{mn}(z) &= \langle I_m(\phi, z) I_n(\phi, z) \rangle_{\phi \in [0, 2\pi]} \\ &= \frac{1}{2\pi} \int_0^{2\pi} d\phi I_m(\phi, z) I_n(\phi, z) \\ &= \frac{1}{4} \left[|U_{mp}(z) U_{nq}(z) + U_{mq}(z) U_{np}(z)|^2 \right. \\ &\quad \left. + I_m^p(z) I_n^p(z) + I_m^q(z) I_n^q(z) \right], \end{aligned} \quad (\text{S5})$$

where $I_m^p(z)$ is the intensity at the m th site for the initial excitation at the p site only. Comparing Eq. S4 and Eq. S5, we can write the relation between the intensity correlation and the photon number correlation as

$$\Gamma_{mn}(z) = 4G_{mn} - I_m^p(z) I_n^p(z) - I_m^q(z) I_n^q(z). \quad (\text{S6})$$

The probability $\mathbf{p}_{m,n}$ of finding one particle at site m and one at n ($n \neq m$) at the output for the input coupling at site p and $q \neq p$ is given by

$$\begin{aligned} \mathbf{p}_{m,n}(z) &= |\langle m, n | U(z) | p, q \rangle|^2 \\ &= \left| \frac{\langle m | \otimes \langle n | + \langle n | \otimes \langle m |}{\sqrt{2}} U(z) \frac{|p\rangle \otimes |q\rangle + |q\rangle \otimes |p\rangle}{\sqrt{2}} \right|^2 \\ &= |U_{mp}(z) U_{nq}(z) + U_{mq}(z) U_{np}(z)|^2 \\ &= \Gamma_{mn}(z). \end{aligned} \quad (\text{S7})$$

When we consider $n = m$, the probability is given by

$$\begin{aligned} \mathbf{p}_{m,m}(z) &= |\langle m, m | U(z) | p, q \rangle|^2 \\ &= \left| \left(\langle m | \otimes \langle m | \right) U(z) \left(\frac{|p\rangle \otimes |q\rangle + |q\rangle \otimes |p\rangle}{\sqrt{2}} \right) \right|^2 \\ &= 2|U_{mp}(z) U_{mq}(z)|^2 = \Gamma_{mm}(z)/2. \end{aligned} \quad (\text{S8})$$

Hence, in the case of two identical particles in the SSH chain, the probability of finding one particle at m and one at n can be written in the following compact form

$$\begin{aligned} |\tilde{\Psi}_{m,n}(z)|^2 &= \Gamma_{mn}(z)/(1 + \delta_{m,n}) \\ &= \frac{1}{(1 + \delta_{m,n})} [4G_{mn} - I_m^p(z) I_n^p(z) - I_m^q(z) I_n^q(z)], \end{aligned} \quad (\text{S9})$$

For the sake of presentation, $|\tilde{\Psi}_{m,n}(z)|^2$ is shown in a square grid in the main text. The modulus square of the two-body wave function is then given by

$$\begin{aligned} |\Psi_{m,n}(z)|^2 &= \Gamma_{mn}(z)/2 \\ &= \frac{1}{2} [4G_{mn} - I_m^p(z) I_n^p(z) - I_m^q(z) I_n^q(z)]. \end{aligned} \quad (\text{S10})$$

with $|\Psi_{m,n}(z)|^2 = |\tilde{\Psi}_{m,n}(z)|^2$. In this case, both indices (m and n) run from 1 to N , where N is the total number of sites in the lattice.

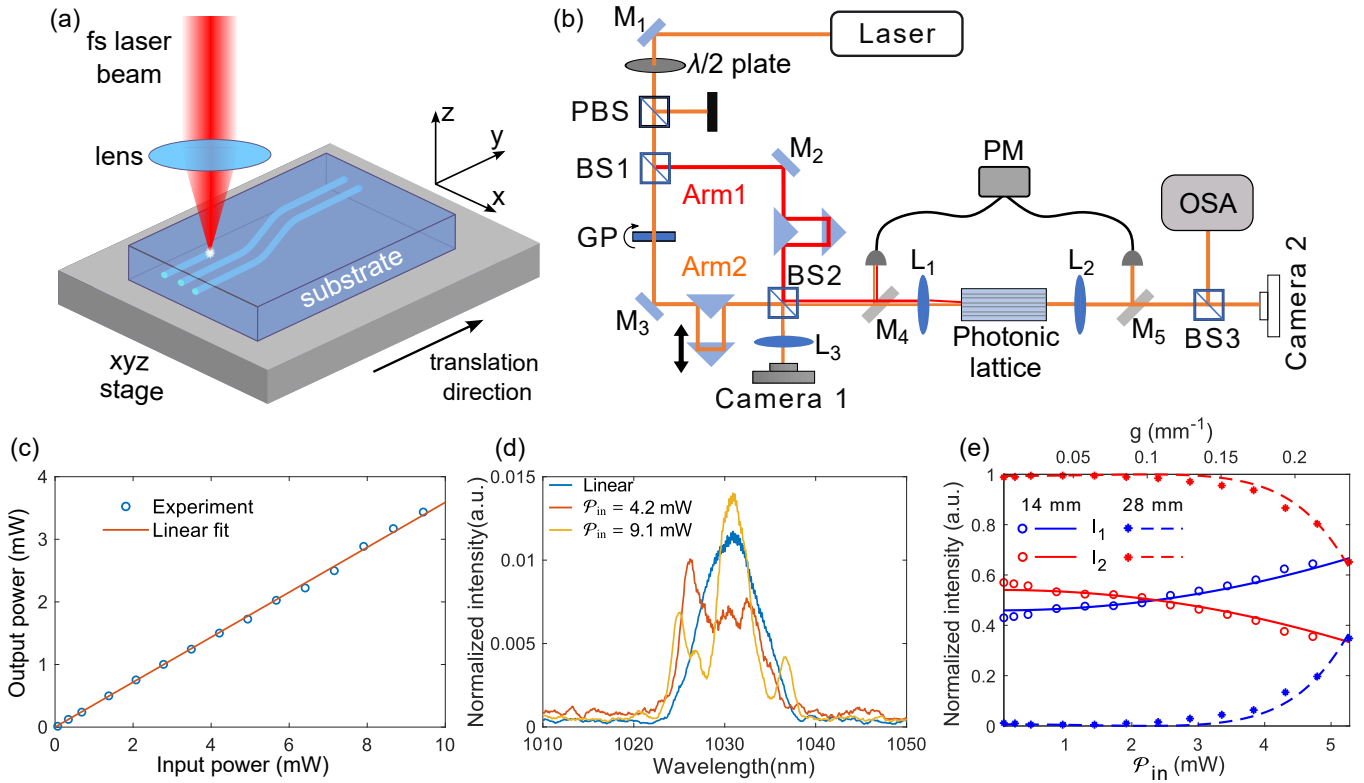


Figure S1. (a) A simplified cartoon of femtosecond laser writing. (b) Experimental set-up for preparing the two-site input state with a tunable relative phase. Here, M_{1-5} are silver-coated mirrors (M_{4-5} are mounted on flip-mounts), BS1-3 are beam splitters, L_{1-3} are convex lenses, PM is a power meter, OSA is an optical spectrum analyzer. The optical delay lines are used to temporally synchronize the laser pulses of arm 1 and arm 2. The relative phase is tuned by rotating a glass plate (GP) mounted on a motorized rotational stage. (c) The variation of average output power as a function of average input power for a typical nonlinear experiment. The linear behavior implies negligible nonlinear loss due to multi-photon absorption processes. (d) Wavelength spectra in the linear and nonlinear regimes. (e) Nonlinear characterization of two straight coupled waveguides with centre-to-centre spacing of $29.5 \mu\text{m}$. Two sets of data correspond to two interaction lengths, $z_{\text{max}} = 14$ mm and 28 mm. The intensity at the waveguide where the light was launched at $z=0$ is denoted by I_1 .

Fabrication and characterization details

In this section, we briefly discuss how the photonic lattices were fabricated and characterized.

Fabrication: Waveguide-based photonic devices were fabricated using femtosecond laser writing [52, 53] – a laser-based technique to modify refractive index inside a transparent and dielectric medium. Optical pulse trains of 260 fs FWHM at 1030 nm central wavelength and 500 kHz repetition rate were generated from a commercially available Yb-doped fiber laser (Satsuma, Amplitude). The power and polarization of the laser beam were controlled by using a polarizing beam splitter and wave plates. For the fabrication purpose, the laser beam with circular polarization was focused (using a 0.4 NA lens) inside a borosilicate (BK7) glass substrate mounted on high-precision x - y - z translation stages (Aerotech Inc.); see Supplementary Fig. S1(a). To create each waveguide, the substrate was translated once through the focus of the laser beam at 6 mm/s speed and 185 mW average power. The translation speed of fabrication and laser power were optimized to

create low-loss single-mode waveguides at a depth of $100 \mu\text{m}$ from the top surface of the substrate. The mode field diameters of the fundamental mode ($1/e^2$ of the intensity peak) were measured to be $25 \mu\text{m}$ and $24.5 \mu\text{m}$ along the vertical and horizontal directions, respectively, at 1030 nm wavelength of light. The propagation loss was estimated by subtracting the coupling losses from the measured insertion loss and was found to be 0.34 dB/cm. The off-diagonal disorder was estimated by characterizing a set of two-waveguide devices with the same inter-waveguide spacing, and was found to be $\Delta J/J = 6\%$. In addition, we observed a nearly full transfer of optical power in such two-waveguide devices, implying that the consisting waveguides have the same onsite energies. In other words, the diagonal disorder is negligible in our experiments.

Characterization set-up: A schematic of the state preparation and device characterization is shown in Supplementary Fig. S1(b). By using a grating pair (not shown in the schematic), near-transform limited 260 fs laser pulses were down-chirped and temporally stretched

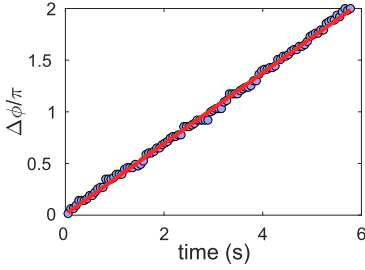


Figure S2. Measured variation of relative phase ϕ as the glass plate shown in Supplementary Fig. S1(b) is rotated with a fixed angular velocity. The solid line is a linear fit. The standard deviation of phase is $\Delta\phi = \pi/30$.

to 1.1 ps. The polarizing beam splitter (PBS) transmits only the horizontal polarization of light whose power was tuned by rotating a $\lambda/2$ plate. The beam is split into two arms using a beam splitter BS1. Optical delay lines are used in both arms to fine-tune the temporal synchronization of the pulses. A 1-mm-thick glass plate (GP) mounted on a motorized rotational stage is placed in arm 2 to control the relative phase ϕ of the optical pulses. Specifically, we rotate the glass plate with a fixed angular velocity to vary the phase ϕ linearly in time with a small standard deviation $\Delta\phi = \pi/30$, as shown in Supplementary Fig. S2.

Laser beams from arms 1 and 2 are reflected and transmitted, respectively, using another beam splitter (BS2). The two beams are then coupled into two desired waveguides using a convex lens (L_1). The interference pattern produced by the two input beams is observed using camera 1, and the intensity distribution at the output of the photonic lattice is imaged on camera 2. During all measurements, the input and output powers were monitored by reflecting the light by the silver-coated mirrors M_4 and M_5 mounted on flip-mounts. The linear variation of the average output power with the average input power implies negligible nonlinear loss due to multi-photon absorption processes; see Supplementary Fig. S1(c). A small fraction of the output power is coupled to an optical spectrum analyzer using the beam splitter BS3 for measuring the wavelength spectrum. In the nonlinear regime, the generation of new wavelength due to self-phase modulation (SPM) is shown in Supplementary Fig. S1(d). Because of temporal pulse shaping, the effect of SPM is minimized – notice that the wavelength span in the nonlinear case is below 15 nm, meaning the wavelength dependence of couplings can be ignored for the maximal power used in our experiments. It should also be noted that the chromatic dispersion is negligible in our experiments because the maximal propagation distance is 80 mm (the dispersion length for BK7 glass is > 50 m).

Estimation of nonlinear strength: As mentioned in the main text, the strength of nonlinearity g is tuned experimentally by varying the laser pulse energy, or

equivalently, the average input power \mathcal{P}_{in} . To get a relation between g and \mathcal{P}_{in} , we characterize nonlinear two-waveguide devices where the dynamics of the optical field is governed by

$$i \frac{\partial}{\partial z} \psi_{1(2)}(z) = -i\alpha\psi_{1(2)} - J\psi_{2(1)} - |\psi_{1(2)}|^2\psi_{1(2)}, \quad (\text{S11})$$

where $\psi_{1(2)}$ is proportional to the slowly-varying complex amplitude of the optical field at the waveguide 1(2). Here, α is a measure of propagation loss, and the evanescent coupling J was measured to be 0.059 mm^{-1} . We considered two devices with the same inter-waveguide spacing $29.5 \mu\text{m}$ and different interaction lengths $z_{\text{max}} = 14 \text{ mm}$ and 28 mm . For all measurements, the light was launched into waveguide 1, i.e., $|\psi_1(z=0)|^2 = 1$, and the variation of normalized intensities at the output of two waveguides are shown in Supplementary Fig. S1(e). For the known value of J and $\alpha = 0.0039 \text{ mm}^{-1}$, we solved Eq. S11 and fitted the experimentally obtained data. The top x-axis in Supplementary Fig. S1(e) indicates the equivalent nonlinear strength, that is used for numerical fitting – the solid and dashed lines. The nonlinear strength g was found to be linearly proportional to the average input power $g = 0.045 \mathcal{P}_{\text{in}} \text{ mm}^{-1} \text{ mW}^{-1}$.

More details on BICs

In the experiments, the BICs were probed by preparing an initial state, $\Psi_{1,3}^{\text{in}} = |1, 3\rangle$ and then observing a large value of $|\Psi_{1,1}|^2$ at the output. We note that the magnitude of $|\Psi_{1,1}|^2$ at a given $J_2/J_1 > 1$ varies as a function of the propagation distance. In fact, $|\Psi_{1,1}|^2$ initially oscillates as a function of z , and then slowly approaches a nonzero value that is determined by the ratio J_2/J_1 . The variation of $|\Psi_{1,1}(z)|^2$ for the experimentally realized values of J_1 and J_2 is shown in Supplementary Fig. S3(a).

Other than the BICs, the initial states $\Psi_{1,3}^{\text{in}}$ has a noticeable overlap with the semi-localized states associated with one particle on the edge and one on the bulk; see Supplementary Fig. S3(b) and Fig. 2(a). However, as mentioned in the main text, the observed large value of $|\Psi_{1,1}|^2$ proves the existence of the BICs. To demonstrate that the large value of $|\Psi_{1,1}|^2$ can not arise due to the excitation of the semi-localized states, we consider another initial state $\Psi_{1,2}^{\text{in}} = |1, 2\rangle$ that has a large overlap (80%) with the semi-localized states; however, it does not excite the BICs; see Supplementary Fig. S3(b). As a result, non-zero elements $|\Psi_{1,n}|^2$ and $|\Psi_{m,1}|^2$ ($m, n \neq 1$) are observed in the experiments with nearly zero magnitude of $|\Psi_{1,1}|^2$; see Supplementary Figs. 2(e, f).

The spatial extent of the BICs is determined by the ratio of J_2 and J_1 – as J_2/J_1 increases, the BICs become more localized. However, the amplitude of the BICs at $\{1, 3\}$ and their overlap with the input state $\Psi_{1,3}^{\text{in}}$ is maximal near $J_2/J_1 = 2.3$. As a result, $|\Psi_{1,1}(z =$

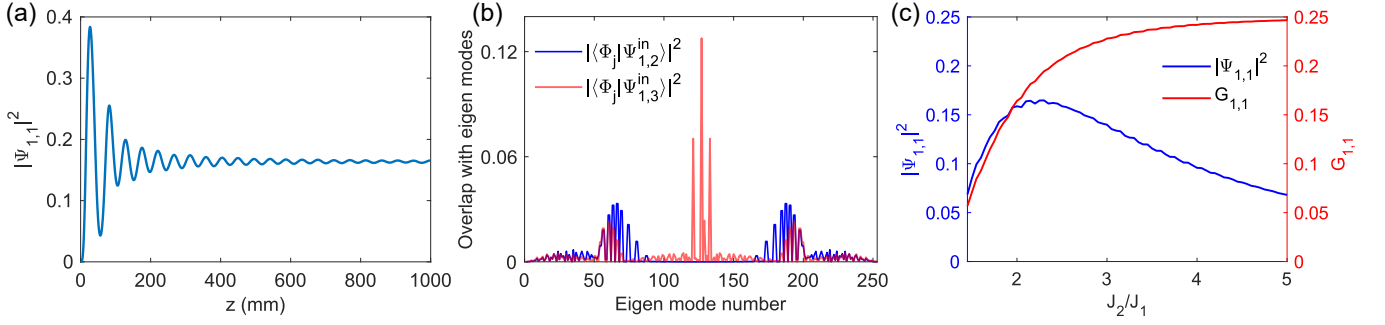


Figure S3. (a) The variation of $|\Psi_{1,1}(z)|^2$ as a function of z for the experimentally realized values of J_1 and J_2 . (b) The overlap of the input state $\Psi_{1,3}^{\text{in}}$ and $\Psi_{1,2}^{\text{in}}$ with the two-body eigenstates ϕ_j . Here, $J_{1,2} = \{0.042, 0.096\} \text{ mm}^{-1}$. (c) The variation of $|\Psi_{1,1}|^2$ and $G_{1,1}$ at $z=1000 \text{ mm}$ as a function of J_2/J_1 .

$1000 \text{ mm})|^2$ exhibits a peak around $J_2/J_1 = 2.3$, as shown in Supplementary Fig. S3(c). For this reason, $J_{1,2} = \{0.042, 0.096\} \text{ mm}^{-1}$ were chosen in experiments to obtain a good signature of the BICs. It should also be noted that unlike $|\Psi_{1,1}|^2$, the intensity correlation at $\{1,1\}$, $G_{1,1}$ increases with J_2/J_1 and then converges to 0.25.

Robustness of BICs.— To inspect the localization feature of the BICs shown in Figs. 2(a), we introduce onsite loss in the middle of the SSH array, Supplementary Figs. S4(a, b). To be more specific, we consider total $N = N_e + N_s = 32$ sites in the array, where $N_s/2 = 10$ sites on both edges are loss-less and $N_e = 12$ sites in the middle have onsite loss $\gamma = J_1/10$. In this situation, all extended eigenstates of the system have a finite imaginary eigenvalue. However, the three BICs possess real eigenvalues, confirming that they are exponentially localized to the edge.

Although BICs can appear in various experimental settings, they are usually fragile states, meaning small perturbations can destroy them. However, the two-body BICs we demonstrate in the main text show remarkable robustness against small disorder. To inspect the robustness of the BICs, we first consider off-diagonal disorder, i.e., disorder in couplings. Each coupling in the lattice is modified as $\tilde{J}_{1,2} = J_{1,2} + \Delta J$, where the random variation in couplings ΔJ is taken from a uniform distribution in the interval $[-\delta J, \delta J]$. As shown in Figs. S4(c, d), the mean value of real as well as imaginary eigenvalues of the BICs are not affected by small coupling disorder. On the other hand, when diagonal disorder (i.e., disorder in onsite energies, $\tilde{\beta} = \beta + \Delta\beta$) is introduced, the BICs become non-degenerate, however, they still remain localized and embedded in the two-body bulk band as long as the disorder strength is small, see Figs. S4(e, f). It should be noted that the width of the middle two-body bulk band is $\pm 2J_1$.

Propagation calculations

In this section, we briefly discuss how the propagation of light is numerically calculated. We consider a 500-mm-

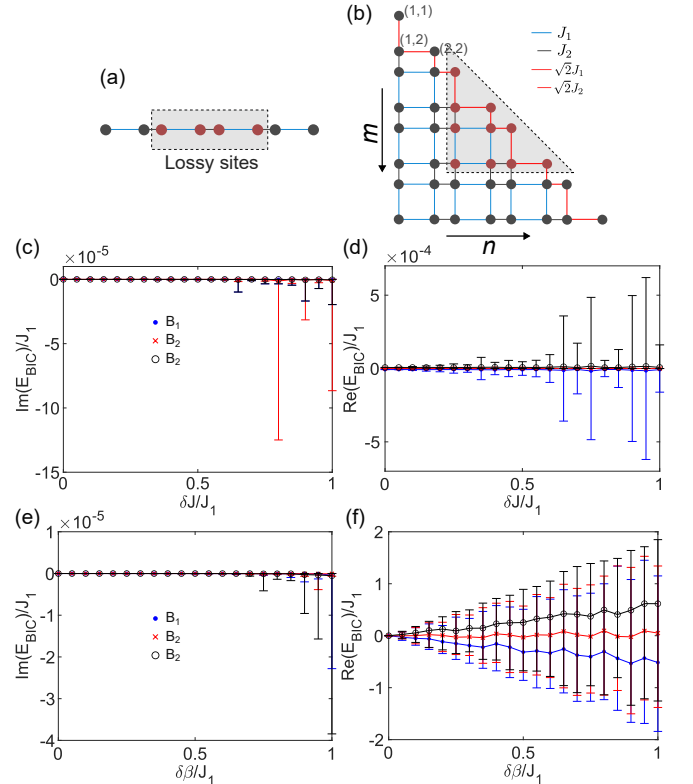


Figure S4. (a) The SSH chain with a total $N = N_s + N_e$ sites where N_e is the number of lossy sites in the middle. $N_s/2$ sites on both edges have zero onsite loss. (b) Two indistinguishable bosons in (a) can be mapped to a single particle in the 2D lattice. (c, d) The variation of the imaginary and real part of the energy of the BICs as a function of coupling disorder. The data points and the error bars indicate the mean and maximum deviation of 100 realizations of disorder. (e, f) Same as (c, d) for the onsite disorder. Here, $J_{1,2} = \{0.042, 0.096\} \text{ mm}^{-1}$.

long SSH lattice of 50 waveguides, which has the same couplings as found experimentally. The linear dynamics is shown in Figs. S5(a-c) [see also Supplementary Movie 1] for input excitation at waveguides 1, and 3 with relative phase $\phi = 0, \pi/2$ and π , respectively – only the first 20 sites are shown here. By varying the relative

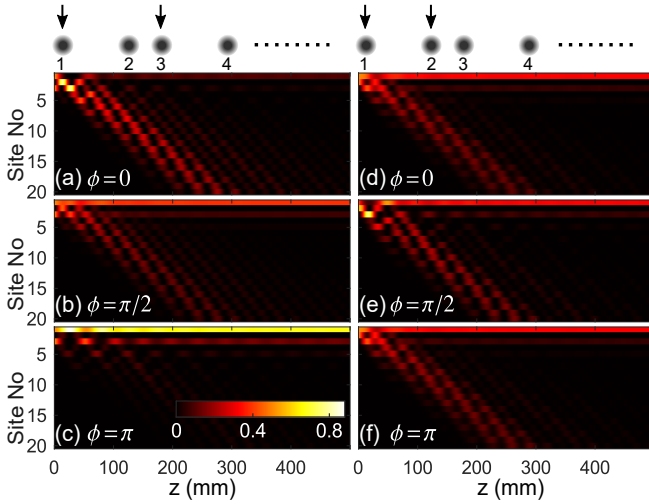


Figure S5. (a-c) The linear dynamics in the SSH lattice when light is coupled to waveguides 1 and 3 (as indicated in the sketch on the top) for 3 different relative phases indicated on each image. The overlap of the input state with the edge states of the SSH lattice is maximal (minimal) for $\phi = \pi$ (0). (d-f) Same as (a-c) for input excitation at waveguides 1 and 2. In this case, the light localized in the edge waveguide does not change with ϕ . In each image, the field of view is smaller than the actual numerics, where 50 waveguides were considered. At all propagation distance the total power is normalized to 1.

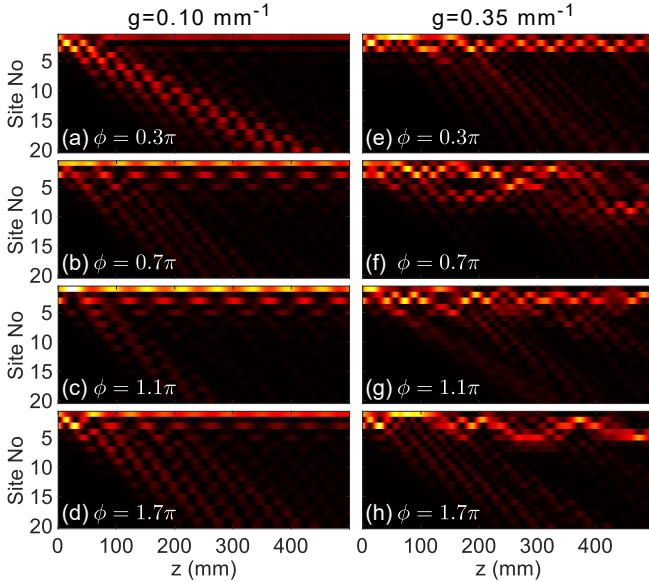


Figure S6. Numerically calculated dynamics of the two-site input state for four different relative phases, $\phi = 0.3\pi, 0.7\pi, 1.1\pi$ and 1.7π indicated on each image. The nonlinear strength is $g = 0.1 \text{ mm}^{-1}$ for (a-d) and $g = 0.35 \text{ mm}^{-1}$ for (e-h). An edge soliton and long-lived breathers are observed in (a) and (b-d), respectively. The light tends not to be maximally localized on the edge site 1 in (e-h). The field of view is smaller than the actual numerics where 50 waveguides were considered. At all propagation distance the total power is normalized to 1. The color-map is same as in Fig. S5.

phase, the overlap of the input state with the edge states

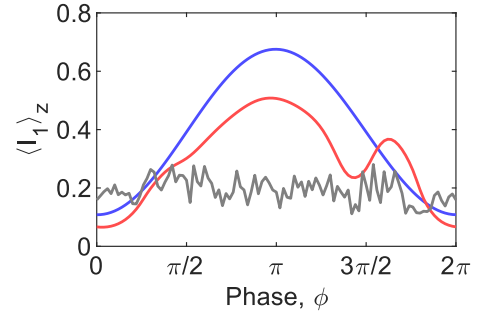


Figure S7. The z averaged intensity of light in waveguide 1 for the linear, weak and strong nonlinear regimes shown by blue, red and grey curves, respectively. Here $z_{\text{max}} = 500 \text{ mm}$.

can be tuned in this case. For example, in the case of $\phi = 0$, a small amount of light remains on the edge because of the small (13%) edge overlap. On the other hand, the edge overlap is large (84%) for $\phi = \pi$, and hence, the light remains localized mostly on the edge. In the experiments presented in Fig. 2(b), we measured output intensities after a propagation of 80 mm, which is in good agreement with the numerical results in Supplementary Figs. S5(a-c).

The linear dynamics for input excitation at waveguides 1, and 2 with three different relative phases are shown in Supplementary Figs. S5(d-f). Irrespective of the phase value, the same amount of light is localized on the edge waveguide. This can be understood from the fact that the edge states of the SSH lattice live on the odd sites (1, 3, 5, ...), as shown in Fig. 1(c). In other words, the overlap between the input state and the edge states does not change as the relative phase is varied.

We now consider the nonlinear dynamics of the two-site input state launched at waveguides 1, and 3 for $g = 0.1 \text{ mm}^{-1}$ and $g = 0.35 \text{ mm}^{-1}$, see Supplementary Fig. S6 and Supplementary Movie 2 and 3. As discussed in the main text, at a weak nonlinear strength $g = 0.1 \text{ mm}^{-1}$, long-lived breathers and solitons are formed at the edge of the lattice for a wide range of relative phase ϕ . Supplementary Figs. S6(a) and (b-d) confirm the formation of edge soliton and breather-like solutions, respectively. In case of Supplementary Fig. S6(a), most of the light ($\approx 75\%$) penetrates the bulk because edge solitons requires relatively low power. As shown in Supplementary Fig. S9, edge solitons break down as the optical power exceeds a threshold value.

For a larger nonlinearity $g = 0.35 \text{ mm}^{-1}$, the light tends not to be maximally localized on the edge site 1 as shown in Supplementary Figs. S6(e-h). Unlike the weak nonlinear regime, in this case, the nonlinear dynamics is extremely sensitive to the relative phase ϕ . It should be highlighted that true breathers can form in the large nonlinear regime as shown in Supplementary Fig. S9.

In the main text, we have presented the variation of intensity at waveguide 1 as a function of phase ϕ .

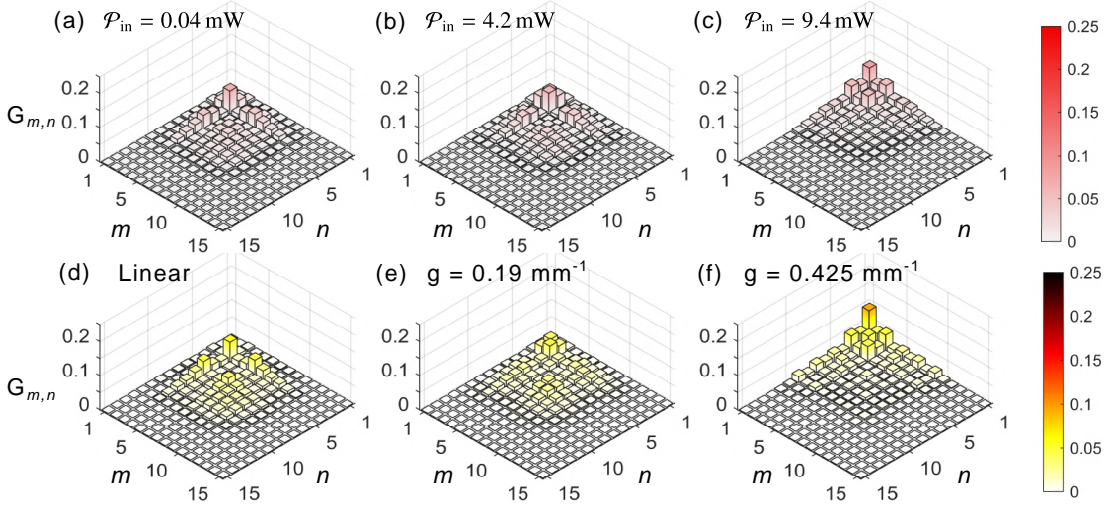


Figure S8. Experimentally measured (a-c) and numerically calculated (d-f) variation of $G_{m,n}$ as a function of nonlinearity for a lattice with homogeneous coupling strength $J=0.046 \text{ mm}^{-1}$. Here, z_{\max} is 80 mm, and the loss coefficient is $\alpha=0.0039 \text{ mm}^{-1}$.

The variations of $I_1(\phi)$ clearly show distinct behavior depending on the strength of the nonlinearity, Fig. 3(e). To show that this behavior is not a z dependent effect, we consider the z averaged intensity of light in waveguide 1, i.e. $\langle I_1 \rangle_z = \frac{1}{z} \int_0^z dz' I_1(z')$. In Supplementary Fig. S7, we show $\langle I_1 \rangle_z$ for three different nonlinear strengths. Notice the appearance of a single peak and a double peak in the linear and weak nonlinear ($g = 0.1 \text{ mm}^{-1}$) regimes respectively. For a large nonlinearity, $\langle I_1 \rangle_z$ fluctuates rapidly with phase, as shown by the grey curve in Supplementary Fig. S7.

Intensity correlations in a homogeneous 1D array

In Fig. S8, we show intensity correlations $G_{m,n}$ for a lattice with homogeneous coupling, $J = 0.046 \text{ mm}^{-1}$. Figs. S8(a-c) show the experimentally obtained correlations, and Figs. S8(d-f) show the corresponding numerical results that are in good agreement with experiments. For this array, there is no state localized on the edge, and hence, $G_{m,n}$ exhibits delocalization in the linear case. As the strength of nonlinearity is increased, the intensity correlations become more localized near the edge. In numerics, we introduced loss by adding a term $-i\alpha\psi_j$ on the right-hand side of Eq. 1, where α is the loss coefficient that was experimentally measured to be $\alpha=0.0039 \text{ mm}^{-1}$.

Discrete breathers

As mentioned in the main text, a discrete breather is a nonlinear state (usually exponentially) localized along the lattice axis and periodic along the propagation distance. Here, we are considering a photonic SSH lattice described by a static, i.e., z -independent linear Hamiltonian \hat{H}^{lin} . When a breather is formed, the nonlinearity locally modifies the onsite energy in a z -periodic manner. In other words, the total Hamiltonian

$\hat{H}_t = \hat{H}^{\text{lin}} + \hat{H}^{\text{nl}}$ is periodic in z with a periodicity of the breather, i.e., $\hat{H}_t(z + z_0) = \hat{H}_t(z)$, where the period $z_0 = 2\pi/\Omega$. It is evident that the Floquet theory can be employed to obtain the breather solution and its quasienergy.

The propagation of optical intensity presented in Supplementary Movie 3 shows breather-like edge modes for a few values of the relative phase ϕ . Inspired by this observation, we use a Floquet self-consistency algorithm [58] to look for true breathers. We consider a finite SSH lattice of 21 sites and experimentally realized values of couplings. Starting from a ‘guess’ solution, we iteratively calculate the breather state, bifurcating from the linear topological edge mode. The quasienergy of the breather and its propagation dynamics is shown in Figs. S9(a, b). The breather is localized on the edge with a periodicity of $z_0 = 25 \text{ mm}$.

Let us now consider the breather-like solutions shown in Fig. 3(f) and Supplementary Movie 2. We note that these solutions are observed for a wide range of relative phases in the propagation calculation. Importantly, the period of such states is observed to be $\approx 58 \text{ mm}$, i.e., more than twice the true breather shown in Fig. S9(b). Now, the periodic nature of the Hamiltonian makes the quasienergy spectrum periodic, i.e., $\varepsilon \in [-\Omega/2, \Omega/2]$. For a long period of 58 mm, the quasienergy spectrum becomes gapless due to band folding. Hence, the breather-like states with long periods of oscillations are in resonance with the linear Floquet modes, causing their finite lifetime. In other words, these breather-like states slowly radiate power into the bulk during propagation.

Breaking of edge soliton: Experiments

A family of edge solitons exists in the topological band gap of the SSH lattice [40]. We numerically obtain the soliton solutions using the self-consistency algorithm. As

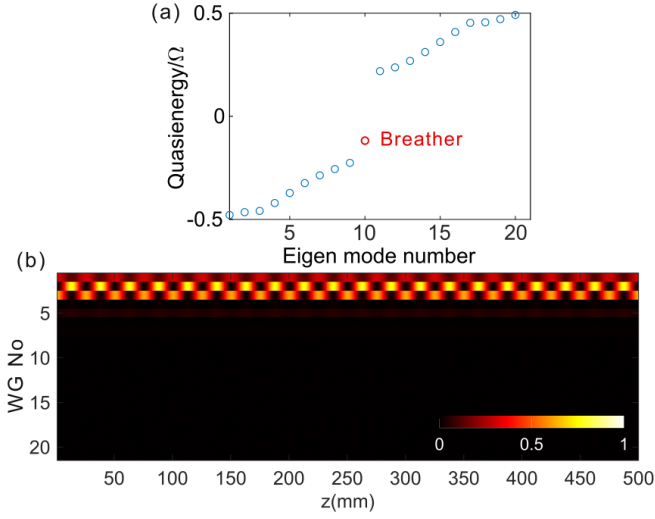


Figure S9. (a) Quasienergy spectrum of the SSH lattice supporting a discrete breather. The linear modes are indicated in blue, and the breather quasienergy is shown in red. (b) Propagation of the breather in (a). Here, the period of the breather is 25 mm, and the nonlinear strength is $g=0.31 \text{ mm}^{-1}$

shown in Fig. S10(a), the edge soliton family bifurcates from the linear edge mode of the SSH lattice. We probe these nonlinear localized modes by coupling light into a single edge waveguide, i.e., site 1. As the nonlinear strength is increased, the energy of the edge soliton reduces and approaches the lower bulk band. As a result, the output intensity pattern remains localized on the edge up to a threshold nonlinear strength, after which the output intensity becomes delocalized. The edge localization is clearly visible in Figs. S10(b,c), and the breaking of edge solitons can be seen in Fig. S10(d).

Description of supplementary movies

[URL for Supplementary Movie 1-3](#)

Supplementary Movie 1.— The linear ($g \rightarrow 0$) propagation of optical intensity in the SSH lattice for the two-site initial excitation at waveguides 1 and 3 with relative phase ϕ indicated on the top. The field of view is smaller than the actual numerics, where 50 waveguides were considered. Here, we have considered experimentally realized values of $J_{1,2}$.

Supplementary Movie 2.— Nonlinear propagation at $g = 0.1 \text{ mm}^{-1}$, otherwise same as Supplementary Movie 1. Notice the formation of long-lived discrete breathers near $\phi = (0.9 \pm 0.4)\pi$ and $\phi = (1.65 \pm 0.1)\pi$.

Supplementary Movie 3.— Nonlinear propagation at $g = 0.35 \text{ mm}^{-1}$, otherwise same as Supplementary Movie 1. Notice that the dynamics is more sensitive to relative phase ϕ , and localized nonlinear edge modes are formed

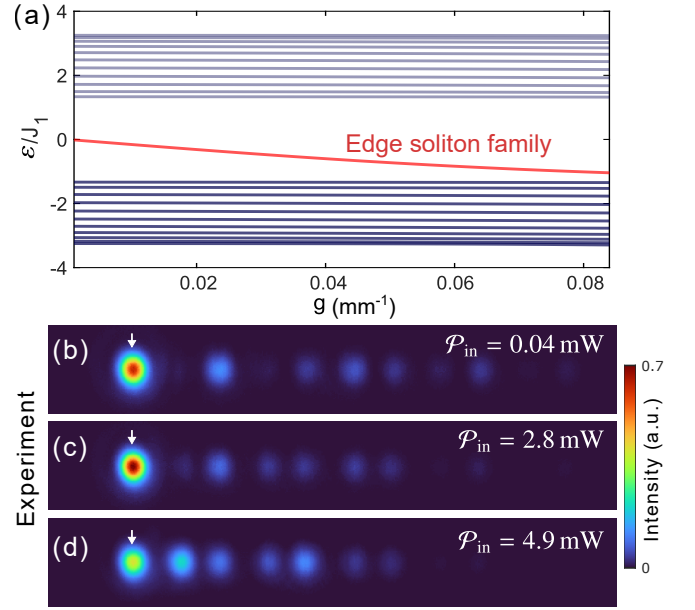


Figure S10. (a) Nonlinear spectrum as a function of renormalized power g showing a family of edge solitons bifurcating from the linear edge mode of the SSH lattice. The linear bulk modes are shown in blue. (b-d) Experimentally measured output intensity distributions at three different input powers. In all three cases, the light was initially launched at waveguide 1 indicated by an arrow. The linear edge mode and an edge soliton are shown in (b) and (c), respectively. The breaking of the edge soliton is shown in (d).

only for a few specific values (not for a wide range) of the relative phase ϕ .